Power Electronic Systems
Laboratory

IEEE Transactions on Industrial Electronics, Vol. 59, No. 5, pp. 2236-2247, May 2012.

50-N · m/2500-W Bearingless Motor for High-Purity Pharmaceutical Mixing

B. Warberger
R. Kaelin
T. Nussbaumer
J. W. Kolar

Eidgenössische Technische Hochschule Zürich
Swiss Federal Institute of Technology Zurich

50-N · m/2500-W Bearingless Motor for High-Purity Pharmaceutical Mixing

Bernhard Warberger, Remo Kaelin, Thomas Nussbaumer, *Member, IEEE*, and Johann W. Kolar, *Fellow, IEEE*

***Abstract*—In this paper, a novel bearingless motor (50 N · m/2.5 kW) for high-purity mixing applications is presented. The motor consists of a stator with concentrated windings and an exterior rotor with permanent magnets. The rotor is propelled and spatially suspended only by means of magnetic fields. This paper deals with the functionality and the mechanical setup of the new motor. Thereby, the optimization of the motor design is presented in detail. In order to evaluate the load of the bearingless motor in mixing operation, a fluid simulation is set up. Moreover, after the identification of the losses, a thermal simulation is established in order to predict the temperature distribution within the motor. Finally, a functional model is built up to verify the results.**

***Index Terms*—Brushless motors, continuous stirred tank reactor, design optimization, eddy currents, fluid dynamics, magnetic forces, magnetic levitation, thermal analysis, torque measurement.**

NOMENCLATURE

B	Radial air gap flux density.
B_{fe}	Flux density in stator teeth.
$c_{\mathrm{fe}}, c_{\mathrm{hy}}, \beta$	Material constants of stator iron.
d_{a}	Outer diameter of agitator.
d_{v}	Diameter of vessel.
D_{wall}	Mean diameter of tube-shaped tank wall.
f_{el}	Electric frequency.
F_x	Bearing force in x-direction.
F_y	Bearing force in y-direction.
g_1, g_2	Geometry proportion factor.
h	Motor height.
h_{a}	Height of agitator.
h_{wall}	Height of tank wall.
I_{BNG}	Bearing current.
I_{DRV}	Drive current.
j	Number of stator iron segments.
K	Overhang correction factor.
k	Number of stator coils.
k_{Fx}	Bearing-current-force factor.
k_T	Drive-current factor.
k_{tilt}	Tilting stiffness.
k_z	Axial stiffness.
m_{fe}	Mass of stator iron.
n	Rotor speed.
N_{coil}	Winding number.
Ne	Newton number or power number.
p	Number of pole pairs.
P_{cu}	Copper losses in stator windings.
$P_{\mathrm{fe}}, P_{\mathrm{ed}}, P_{\mathrm{hy}}$	Iron, eddy-current, and hysteresis losses.
P_{tot}	Total losses.
P_{wall}	Eddy-current losses in the tank wall.
R_{cu}	Ohmic resistance of one stator coil.
Re	Reynolds number.
r_{i}	Inner rotor radius.
r_{o}	Outer rotor radius.
T	Rotor torque.
w_{s}	Width of stator teeth.
x, y, z	Spatial coordinates.
α_{a}	Mixer blade pitch.
α_{el}	Electric angular rotor position.
α_{mech}	Mechanical angular rotor position.
Δ_r	Radial rotor dislocation.
Δ_x, Δ_y	Rotor dislocation in x- and y-directions.
Δ_z	Axial rotor dislocation (z-direction).
δ_{er}	Thickness of motor encapsulation.
δ_{es}	Thickness of stator encapsulation.
δ_{fluid}	Thickness of fluid gap.
δ_{mag}	Thickness of magnetic gap.
δ_{pm}	Thickness of permanent magnets.
δ_{r}	Rotor ring thickness.
δ_{wall}	Thickness of tank wall.
Θ	Magnetomotive force (MMF).
$\Theta_{\mathrm{max,c}}$	Maximal MMF with two water-cooling helixes.
$\Theta_{\mathrm{max,nc}}$	Maximal MMF without additional water cooling.
$\Theta_{\mathrm{max,sc}}$	Maximal MMF with one water-cooling helix.
ϑ_{cu}	Temperature of stator windings.
ϑ_{PCB}	Maximal temperature of printed circuit board (PCB).
ϑ_{S}	Temperature of position sensor.
μ	Harmonic number.
ν	Dynamic viscosity of process fluid.
ξ	Overhang factor.
ρ	Density of process fluid.
σ	Electric conductivity of the tank wall.
ω_{el}	Electric angular velocity.
$\hat{}$	Indicating peak values (amplitude).

Manuscript received February 1, 2011; revised April 15, 2011 and May 30, 2011; accepted June 1, 2011. Date of publication July 14, 2011; date of current version February 3, 2012.

B. Warberger is with the Power Electronic Systems Laboratory, Swiss Federal Institute of Technology (ETH) Zurich, 8005 Zurich, Switzerland (e-mail: warberger@lem.ee.ethz.ch; www.pes.ee.ethz.ch).

R. Kaelin is with BKW-FMB Energy AG, 3013 Bern, Switzerland (e-mail: rkaelin@ee.ethz.ch).

T. Nussbaumer is with Levitronix GmbH, 8005 Zurich, Switzerland (e-mail: nussbaumer@levitronix.com).

J. W. Kolar is with the Power Electronic Systems Laboratory, Swiss Federal Institute of Technology (ETH) Zurich, 8005 Zurich, Switzerland (e-mail: kolar@lem.ee.ethz.ch).

Color versions of one or more of the figures in this paper are available online at http://ieeexplore.ieee.org.

Digital Object Identifier 10.1109/TIE.2011.2161657

I. Introduction

THE bearingless slice motor was developed by Schoeb and Barletta [1]. With this technology, contact-free rotation and spatial suspension of a disk- or ring-shaped rotor can be achieved. Meanwhile, this motor concept has been successfully implemented in various commercially available products (e.g., high-purity pumps or contact-free wafer processing tools [2]–[4]).

Another seminal field of application could be the pharmaceutical or food industry, particularly the mixing of high-purity and delicate fluids.

The aforementioned industry branches normally use stirred vessels for mixing applications. The simplest setup is a mixer with an agitator mechanically connected to a shaft. The drawback is that, where the shaft is penetrating the tank wall, a sealing and a mechanical bearing must be installed.

Leakages, lubricants, and mechanical wear can contaminate the process fluid. Due to the very small gap close to the mechanical bearing, high sheer forces arise, which can cause enduring damage to delicate process fluids or cell cultures [5].

A more advanced approach is the installation of magnetic couplings in order to transmit the torque to the agitator inside the vessel. With this technology, a hermetic encapsulated tank design is enabled. Nevertheless, there is still a need for a mechanical bearing to spatially suspend the impeller inside the tank. Commonly, sliding-contact bearings with ceramic contact surfaces are used [6]. Mechanical wear is reduced but cannot be excluded. Other drawbacks are the very small fluid gap between the sliding surfaces and the very poor dry-running capability, which can become a problem during tank draining or during the cleaning in place and the sterilization in place (SIP) process [7].

To overcome all these handicaps and to meet the tightened purity requirements of the aforementioned industry branches, a mixer topology based on the bearingless slice motor can be implemented. Here, the stator is placed outside the hermetic encapsulated tank. The impeller inside the tank is rotated and spatially suspended by means of magnetic fields. The possible large fluid gap of several millimeters reduces the sheer forces in the bypassing fluid, and mechanical wear can be excluded. Moreover, this design exhibits unlimited dry-running capability.

In principle, two setups of bearingless mixer motors are thinkable (cf. Fig. 1): a bearingless motor with an interior rotor disk or a setup with an exterior rotor ring. The latter design was chosen due to the advantage that the convexity, which accommodates the stator, is pointing inside the tank. Therefore, after draining or cleaning the tank, fluid residues can be excluded.

So far, outer rotor motors, mostly brushless dc motors or permanent-magnet synchronous machines (PMSMs), are typically used for electric vehicles (direct drives [8]–[11]), for wind turbines [12], for fans and blowers [13], or for DVD and hard-disk drives [14]. In all these applications, mechanical bearings are used to spatially suspend the rotor. These mechanical bearings must be eliminated to successfully apply a PMSM in high-purity mixing systems. Information about the setup and the functional principle of bearingless motors can be found in the literature [15]–[19], and in [20], a principle approach of a bearingless slice motor with an exterior rotor is introduced. The first practical industrial application of a bearingless PMSM with an outer rotor for mixing purposes is presented in [21]. Here, the motor is successfully implemented in a 300-W bioreactor mixing system.

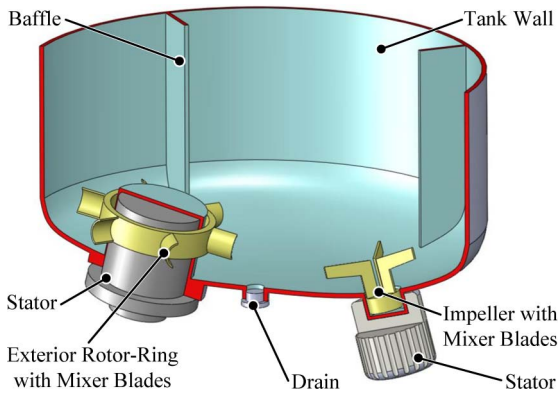

Fig. 1. Principal implementation of a bearingless motor in a stirred vessel: On the left side, a bearingless motor with exterior rotor (preferred design) is shown, and on the right side, a bearingless motor with interior rotor is depicted.

The possibility of an implementation of a bearingless motor with a large magnetic gap (5 mm) in a large scale mixing system (2.5 kW) has not been investigated so far. The interaction between the shape of the contact-free suspended agitator and the occurring fluid forces cannot be found in the literature and must be determined by means of fluid simulation in order to find an optimal combination of the agitator and motor. Moreover, due to the compact design and high torque, the thermal stress of the system components needs to be studied—particularly the heat exchange with the process fluid and the necessity of an additional cooling system.

In this paper, a bearingless motor with an exterior rotor is presented. The motor should be applicable in high-purity mixing vessels of up to 10 000 L. Here, the required torque is about 50 $\mathrm{N \cdot m}$ up to an operation speed of 500 $\mathrm{min^{-1}}$. In Section II, the mechanical setup and functional principle of the bearingless motor with an exterior rotor are explained. Section III contains the design optimization of the motor based on 3-D finite elements method (FEM) simulations. Here, the influence of various design parameters on the motor performance is described, and in Section IV, the optimized design is verified by a prototype. In order to estimate the necessary torque at various mixing speeds, a fluid simulation [3-D computational fluid dynamics (CFD)] was set up. With the simulation model shown in Section V, also the backlash on the motor caused by the fluid and the agitator blade design is investigated. In Section VI, a thermal simulation of the mixer motor is introduced. Due to the high currents and the limited winding space, the necessity of an additional cooling system is investigated. Moreover, during the sterilization process (SIP, 130 °C), the motor, particularly the implemented electronic parts, must be prevented from being damaged by overtemperature.

II. Setup and Functional Principle

In Fig. 2, the mechanical setup of the bearingless mixer motor is depicted. The stator consists of a laminated iron

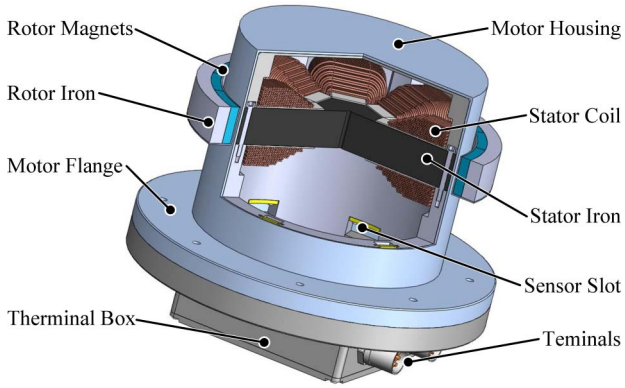

Fig. 2. Mechanical motor setup of the bearingless mixer motor.

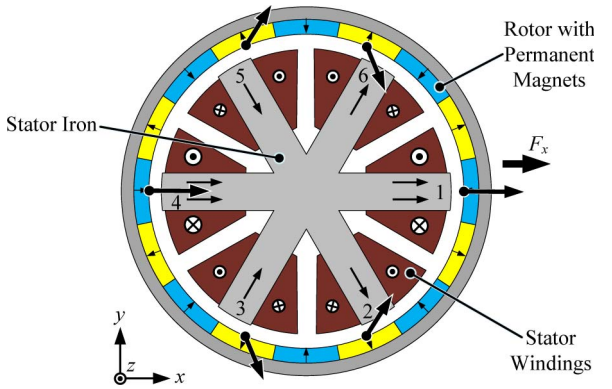

Fig. 3. Schematic top view on rotor and stator illustrates the bearing force generation in the x-direction at a rotational angle of $\alpha_{\mathrm{el}} = 0°$. Always two opposing stator coils are supplied by bearing currents with the same magnitude, but with different signs. One can see that the magnetic forces in the y-direction annihilate each other and only a resultant force F_x in the x-direction remains.

core with six stator teeth and six stator windings. The rotor is composed of a back iron ring with 16 permanent magnets. The stator is mechanically connected to the motor flange and is protected by a thin motor housing. The sensors for detecting the rotational and the radial position of the rotor are embedded in the corresponding sensor slots.

The coils on the stator teeth 1, 3, and 5, as well as those on the teeth 2, 4, and 6 (cf. Fig. 3), are connected in star and constitute two separated three-phase systems which are fed by two half-bridge modules.

With proper current feed of the six coils, active and independent control of three degrees of freedom (DOFs), namely, the translation in the x- and y-directions and the rotation about the z-axis, is possible. The three remaining DOFs (translation in the z-direction and rotation about the x- and y-axes) are stabilized passively by reluctance forces. The magnitude of the reluctance forces is primarily determined by the geometric design of the motor.

The generation of bearing forces and torque is described in great detail in [22]–[24]. Here, an excerpt of the essential information is presented.

A. Bearing Forces

In order to levitate the rotor, the actual rotor position is measured with sensors, and the motor control unit sets the appropriate radial bearing forces F_x and F_y by impressing a bearing current I_{BNG} into the stator windings. It is obvious that the bearing current depends on the actual electric rotor position

$$\alpha_{\mathrm{el}} = p \cdot \alpha_{\mathrm{mech}} \tag{1}$$

which can be calculated by multiplying the mechanical rotor angle α_{mech} and the pole pair number p. The contribution of the stator coil k to the resultant bearing force in the x-direction is

$$F_{x,k}(\alpha_{\mathrm{el}}) = k_{Fx,k} \cdot \cos(\alpha_{\mathrm{el}} + (k-1) \cdot 60°) \cdot N_{\mathrm{coil}} \cdot \hat{I}_{\mathrm{BNG}}. \tag{2}$$

Thereby, $k_{Fx,k}$ is the bearing-current-force factor of coil k in the x-direction, N_{coil} is the winding number, and $\hat{I}_{\mathrm{BNG}}$ is the amplitude of the bearing current. The resultant bearing force in the x-direction is

$$F_x = \sum_{k=1}^{6} F_{x,k}. \tag{3}$$

The bearing force in the y-direction F_y can be calculated accordingly. In Fig. 3, an exemplary constellation of the generation of a bearing force in the x-direction at a rotor angle of $\alpha_{\mathrm{el}} = 0°$ is illustrated.

B. Torque

In order to make the rotor spin, a torque about the z-axis must be generated by impressing a drive current in the stator windings. Similar to the bearing force generation, each coil k contributes a fractional torque

$$T_k(\alpha_{\mathrm{el}}) = k_T \cdot \sin^2(\alpha_{\mathrm{el}} + (k-1) \cdot 120°) \cdot N_{\mathrm{coil}} \cdot \hat{I}_{\mathrm{DRV}} \tag{4}$$

to the total torque

$$T = \sum_{k=1}^{6} T_k = 3 \cdot k_T \cdot N_{\mathrm{coil}} \cdot \hat{I}_{\mathrm{DRV}}. \tag{5}$$

Here, k_T is the drive-current factor and $\hat{I}_{\mathrm{DRV}}$ is the amplitude of the drive current. In Fig. 4, an exemplary constellation of torque generation is depicted.

The simultaneous generation of bearing forces and torque is put into effect by superimposing the corresponding control commands for the power modules.

Another option would be two separated coils per stator tooth, one for torque generation (supplied with I_{DRV}) and one for bearing force generation (supplied with I_{BNG}). This approach was abandoned because of the higher complexity of the system (12 coils instead of 6 coils) and the higher copper losses [25].

III. Design Optimization

When optimizing the motor geometry, not only the torque generation is an important criterion but also the tilting about the x- and y-axes and the translation in the z-direction. The latter three DOFs have a huge impact on the stability of the mixer motor. The passive reluctance forces counteracting tilting

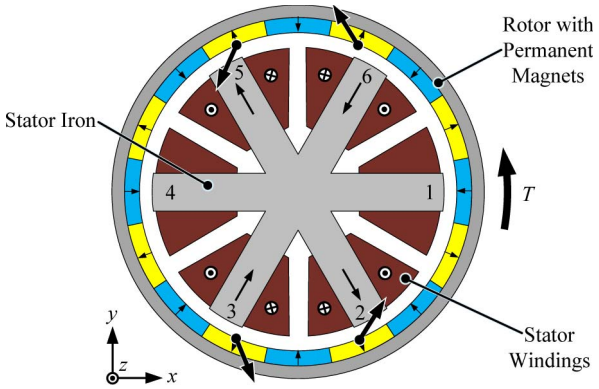

Fig. 4. Schematic top view on the motor shows the torque generation at a rotational angle of $\alpha_{\mathrm{el}} = 0°$. Always two opposing stator coils are supplied by drive currents with the same magnitude and phase. The radial components of the magnetic forces due to the drive current annihilate each other, and the remaining tangential components result in the total torque T.

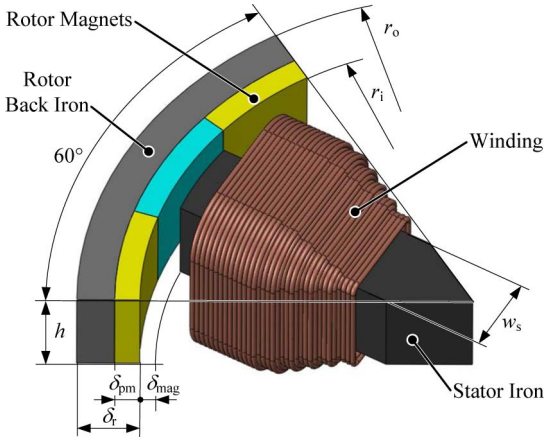

Fig. 5. Geometry definitions of the bearingless mixer motor. The picture shows a 60° section of the motor. During the optimization process, the values for the magnetic gap $\delta_{\mathrm{mag}} = 5$ mm, the motor height $h = 30$ mm, and the outer rotor diameter $r_{\mathrm{o}} = 119$ mm were kept constant.

and axial displacement (tilting stiffness k_{tilt} and axial stiffness k_z) are determined by the geometry of the magnetic circuit. Therefore, during the optimization process, the effects of design variations on k_{tilt} and k_z must be evaluated carefully.

Before optimizing the dimensions of the magnetic circuit, the number of pole pairs of the rotor p and the number of stator teeth must be determined. Previous investigations reveal that a combination of 16 rotor magnets $(p = 8)$ and six stator teeth is optimal for the presented motor concept [22], [23].

With this setup, a high winding factor and a constant torque [cf. (5)] are obtained. Moreover, the cogging torque is low, and the six coils on the six stator teeth can conveniently be supplied by two three-phase modules.

A. Definition of Design Parameters

In Fig. 5, the design parameters of the bearingless motor are depicted. The rotor with the outer radius r_{o} and the thickness δ_{r} consists of a back iron ring and 16 permanent magnets with a thickness of δ_{pm}. The inner rotor radius (air gap radius) is

$$r_{\mathrm{i}} = r_{\mathrm{o}} - \delta_{\mathrm{r}}. \tag{6}$$

The height (elongation in the z-direction) of the motor is h. The width of the stator teeth is denoted as w_{s}. The magnetic gap between the rotor and the stator is δ_{mag}. The thickness of the rotor encapsulation is $\delta_{\mathrm{er}} = 1$ mm, the thickness of the stator encapsulation is $\delta_{\mathrm{es}} = 1$ mm, and the tank wall thickness is $\delta_{\mathrm{wall}} = 1$ mm. In order to keep the fluid sheer forces low, a fluid gap of $\delta_{\mathrm{fluid}} = 2$ mm should be maintained. Therefore, the magnetic gap results in

$$\delta_{\mathrm{mag}} = \delta_{\mathrm{fluid}} + \delta_{\mathrm{er}} + \delta_{\mathrm{es}} + \delta_{\mathrm{wall}} = 5 \text{ mm}. \tag{7}$$

As derived in [26] in detail, the torque

$$T|_{h=\mathrm{const.}} \propto r_{\mathrm{i}}^3 \tag{8}$$

depends highly on the radial dimension of the motor. Therefore, the torque can easily be raised by increasing the diameter of the motor. However, to achieve good mixing, the size of the rotor must be proportioned to the vessel size (see Section V). According to existing mixer tank designs [6], the outer radius of the rotor was set to $r_{\mathrm{o}} = 119$ mm in order to make the motor suitable for a 5000–10 000-L vessel.

When examining the motor setup, it arises that the achievable torque T is increasing with the motor height h. Contrariwise, the tilting stiffness k_{tilt} is reduced by increasing h. As will be shown later, with $h = 30$ mm, the maximal tilting stiffness is provided under the condition that the targeted torque is achievable.

In order to calculate the motor torque, a specific value of the MMF

$$\Theta = N_{\mathrm{coil}} \cdot I_{\mathrm{DRV}} \tag{9}$$

has to be assumed. Θ is limited by the maximal allowable temperature in the mixer motor. Based on the thermal simulation presented in Section VI, the maximal MMF for a water-cooled motor (full load) can be set to $\Theta_{\mathrm{max,c}} = 5000$ At., but without additional water cooling, the maximal MMF must be reduced to $\Theta_{\mathrm{max,nc}} = 0.4 \cdot \Theta_{\mathrm{max,c}}$.

B. Optimization of Geometry Parameters

As described earlier, the outer rotor radius r_{o}, the motor height h, and the magnetic gap δ_{mag} are already fixed. The remaining free design variables are the inner rotor radius r_{i}, the stator tooth width w_{s}, and the magnet thickness δ_{pm}.

In a first step, the influence of the inner rotor radius r_{i} and the magnet thickness δ_{pm} on the achievable torque is investigated. When varying r_{i}, a clear optimum is expected. If r_{i} is below the optimal value, the torque is reduced according to (8) which cannot be compensated by the increasing rotor thickness $\delta_{\mathrm{r}} = r_{\mathrm{a}} - r_{\mathrm{i}}$ and the proportional increasing magnet thickness δ_{pm}, respectively. On the other hand, if r_{i} is too high, the torque is reduced due to the small remaining rotor thickness δ_{r} and the accordingly smaller magnet thickness δ_{pm}.

If r_{i} is fixed to a certain value and only a variation of the magnet thickness δ_{pm} is examined, also a clear optimum can be expected. It is obvious that the torque is increased by rising δ_{pm}. Otherwise, if δ_{pm} is too large, the remaining back iron

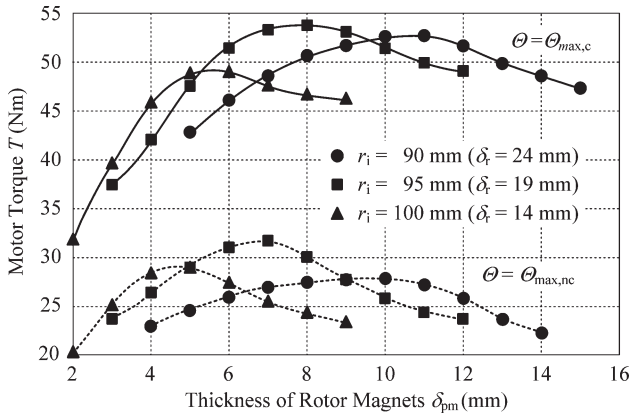

Fig. 6. Achievable motor torque in dependence on the inner rotor radius r_i and the rotor magnet thickness δ_pm. $\Theta_\mathrm{max,c}$ is the maximal MMF with water cooling, and $\Theta_\mathrm{max,nc}$ is the maximal MMF without additional cooling.

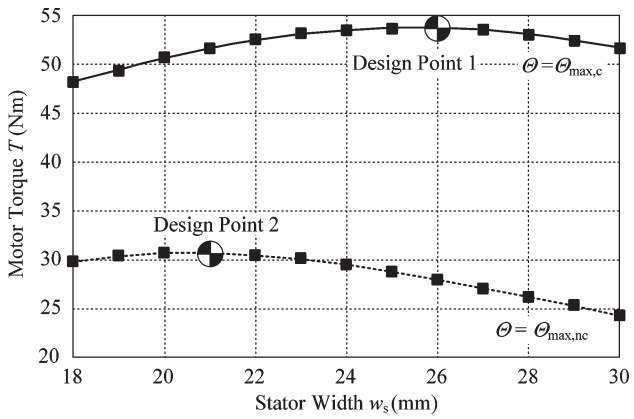

Fig. 7. Achievable motor torque T in dependence on the stator width w_s for a water-cooled and a noncooled motor.

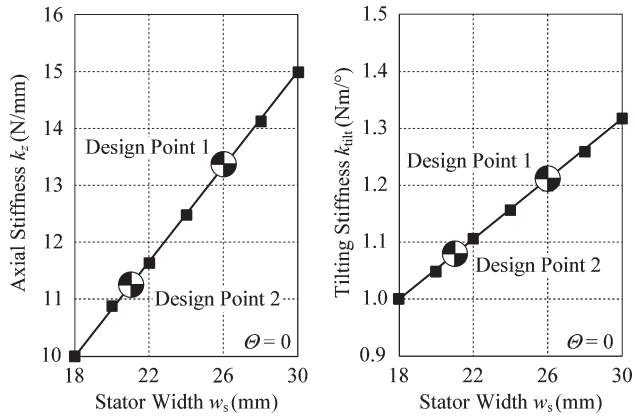

Fig. 8. Axial stiffness k_z and tilting stiffness k_tilt in dependence on the stator tooth width w_s.

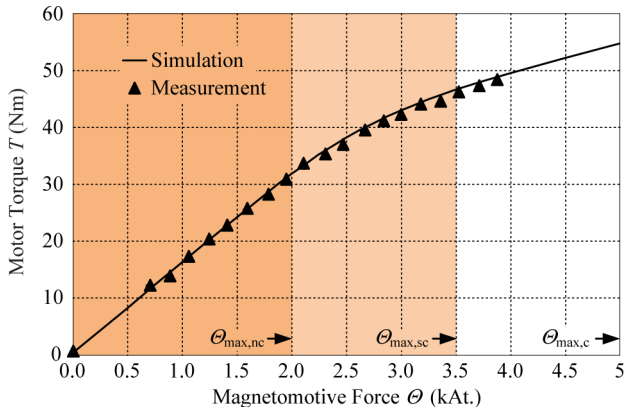

Fig. 9. Simulated torque and measured torque in dependence on the MMF. $\Theta_\mathrm{max,c}$ is the maximal allowable MMF with two cooling helixes, and $\Theta_\mathrm{max,sc}$ is the maximal allowable MMF with only one cooling helix. Without additional cooling, the maximal MMF is $\Theta_\mathrm{max,nc}$.

ring gets smaller and saturates. Thus, the stronger magnets do not result in higher magnetic flux and torque, respectively.

To find the optimum, various combinations of r_i and δ_pm have been simulated [27]. In Fig. 6, the results of this optimization step are depicted. It arises that the highest torque is achieved with an inner rotor radius of $r_\mathrm{i} = 95$ mm. The optimal magnet thickness is within $\delta_\mathrm{pm} = 7$ mm $\ldots$ 8 mm, depending on the level of applied ampere-turns. Finally, it was set to $\delta_\mathrm{pm} = 7$ mm.

The last remaining design variable is the stator tooth width w_s. In Fig. 7, the coherence between w_s and the motor torque T is depicted. One can see that there is an optimum for a water-cooled motor (design point 1) and an optimum for the motor without additional cooling (design point 2). As expected, due to the higher MMF $\Theta_\mathrm{max,c}$ in design point 1, the stator width w_s must be larger than that in design point 2 to avoid saturation.

In order to decide whether the geometry should be optimized for a water-cooled or noncooled setup, the effect of the stator width w_s on the axial stiffness k_z and on the tilting stiffness k_tilt was evaluated. In Fig. 8, the results of this investigation are depicted. It arises that both k_z and k_tilt are increased by a wider stator tooth. Therefore, design point 1 was chosen, and the stator width was set to $w_\mathrm{s} = 26$ mm.

IV. Verification of the Optimized Design

According to the optimal geometry dimensions defined in Section III, a laboratory prototype was set up and was put to operation successfully. First of all, the static torque was measured and compared to the simulated results. In Fig. 9, the achievable static motor torque in dependence on the MMF is depicted. As described in Section VI, the maximal MMF must be limited to avoid the overheating of the motor. Without a cooling system ($\Theta_\mathrm{max,nc}$), a torque of about 32 N $\cdot$ m is achievable.

With one activated cooling helix ($\Theta_\mathrm{max,sc}$), the maximal torque is about 47 N $\cdot$ m, and with two cooling helixes ($\Theta_\mathrm{max,c}$), the maximal torque is about 54 N $\cdot$ m.

During mixing operation, remarkable axial forces can act on the rotor (cf. Section V). Therefore, the axial restoring force F_z was examined in detail. The comparison depicted in Fig. 10 reveals that the measured and simulated values of F_z match very well.

During the design optimization, only the static torque has been considered. However, during operation, eddy currents are induced in the metallic tank wall which is placed in the magnetic gap and therefore penetrated by the alternating radial flux density B (see Section VI). This electric conductible tank wall acts like an eddy-current brake, and the maximal motor

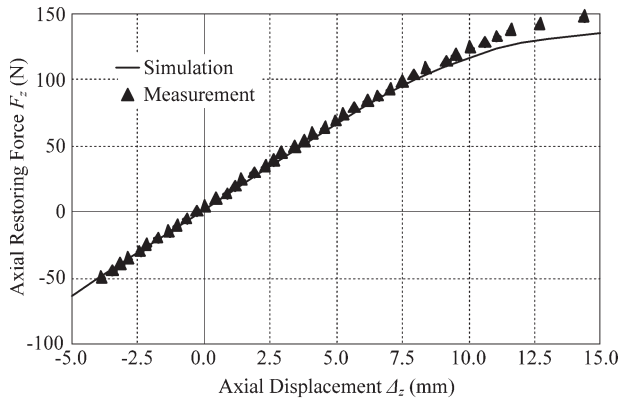

Fig. 10. Comparison of the simulated and the measured axial restoring force F_z. The preload due to the own weight of the rotor was considered in the simulation.

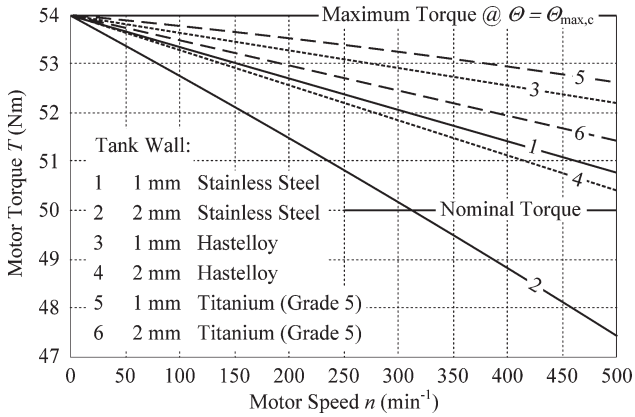

Fig. 11. Torque reduction due to eddy-current losses in the metallic tank wall in dependence on wall material, wall thickness, and motor speed ($\Theta = \Theta_{\mathrm{max,c}}$).

torque is reduced. In Fig. 11, the maximal possible motor torque at $\Theta_{\mathrm{max,c}}$ in dependence on motor speed, wall material (conductivity), and wall thickness is depicted. It can be seen that the maximal torque is reduced, but the nominal torque of 50 N · m at 500 min^{-1} can be archived with various tank wall materials.

Finally, the presented mixer motor was tested during operation. The motor was accelerated to the nominal speed $n = 500$ min^{-1} and afterward slowed down to a standstill. The radial displacement $\Delta_{\mathrm{r}}(t)$ and the drive current $i_{\mathrm{DRV}}(t)$ are depicted in Fig. 12. The maximal radial rotor dislocation observed during operation was only $\Delta_{\mathrm{r}} = \pm 200\ \mu$m.

V. Fluid Forces

A. Fluid Simulation

In order to estimate the forces acting on the agitator in the mixing operation, a finite-element fluid simulation (3-D CFD, [28]) was set up. Moreover, this simulation should show which principle agitator design is suitable for the bearingless mixer motor. As described in Section VI, the process fluid is also used for cooling the motor. To estimate the cooling effect of the bypassing fluid, the knowledge of the flow profile around the motor is essential.

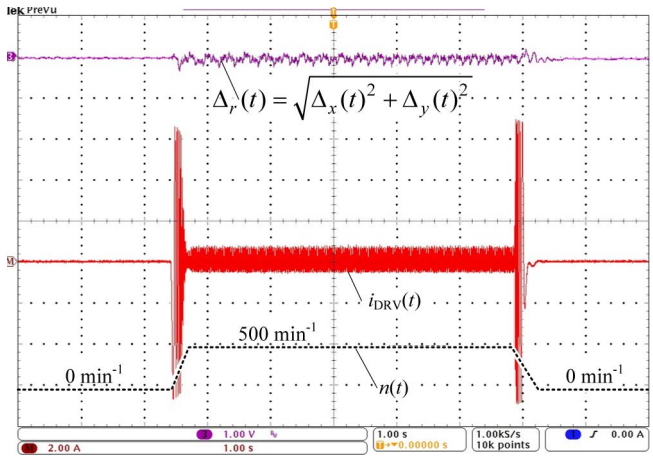

Fig. 12. Radial displacement $\Delta_{\mathrm{r}}(t)$ and drive current $i_{\mathrm{DRV}}(t)$ during an acceleration up to 500 min^{-1} and a brake down to a standstill (displacement scale of 0.5 mm/div, current scale of 2 A/div, and time scale of 1 s/div).

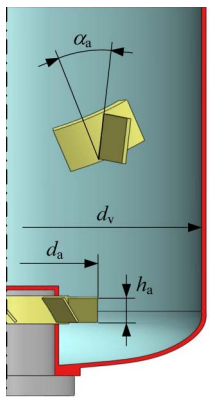

Setup	h_a (mm)	d_v (mm)	d_a (mm)	α_a (°)
1	60	1200	270	0.0
2	60	1200	310	0.0
3	60	1200	350	0.0
4	60	1200	350	22.5
5	60	1200	350	45.0
6	60	1200	350	67.5

d_v Diameter of Vessel
d_a Outer Diameter of Agitator
h_a Height of Agitator
α_a Mixer Blade Pitch

Fig. 13. (Left) Definition of mixer dimensions and (right) overview of simulated agitator setups.

As depicted in Fig. 13, six different agitator setups were simulated. Thereby, two standard agitator types were evaluated, namely, the pitched-blade agitator (blade pitch $\alpha_{\mathrm{a}} > 0°$, cf. Fig. 13) and the flat-blade agitator ($\alpha_{\mathrm{a}} = 0°$). When defining the mixer dimensions, the proportion factor

$$g_1 = \frac{d_{\mathrm{a}}}{d_{\mathrm{v}}} \approx (0.2 \ldots 0.4) \tag{10}$$

between the diameter of the vessel d_{v} and the outer diameter of the agitator d_{a} and the factor

$$g_2 = \frac{h_{\mathrm{a}}}{d_{\mathrm{a}}} \approx 0.2 \tag{11}$$

between blade height h_{a} and agitator diameter d_{a} should be respected to achieve good mixing process performance [29].

In Fig. 14, the characteristic flow patterns of a mixer setup with a pitched-blade (left) and a flat-blade agitator (right) are shown. Each mixing process can be defined by two dimensionless numbers.

First, the Newton number (power number)

$$Ne \equiv \frac{2 \cdot \pi \cdot T}{\rho \cdot n^2 \cdot d_{\mathrm{a}}^5} \tag{12}$$

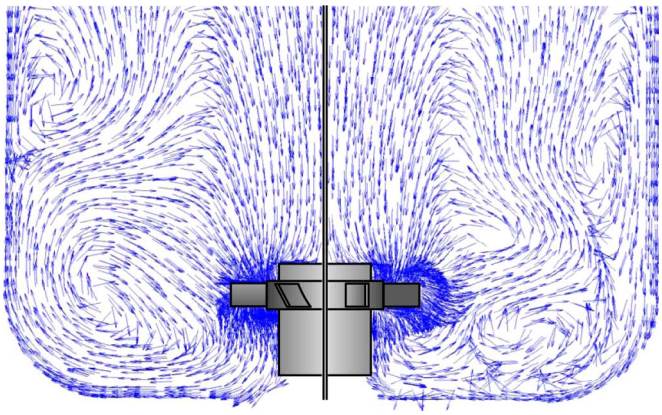

Fig. 14. Characteristic flow pattern of (left) a clockwise rotating pitch-blade agitator and (right) a flat-blade agitator.

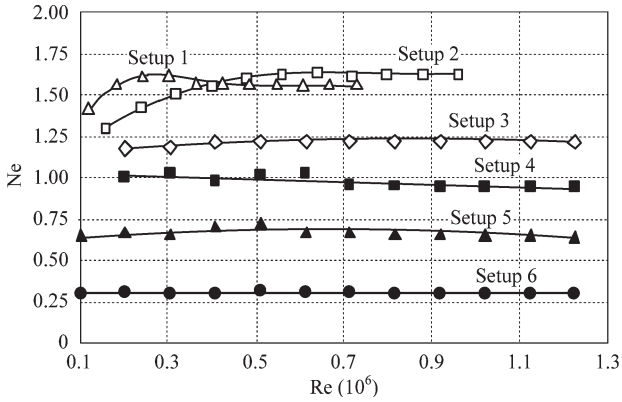

Fig. 15. Simulated power characteristics $\mathrm{Ne} = f(\mathrm{Re})$ of the investigated agitator setups (the parameters of the agitator setups are listed in Fig. 13).

is composed of the mixer load torque T, the fluid density ρ, the rotational speed n, and the outer agitator diameter d_a.

The second dimensionless number is the Reynolds number

$$\mathrm{Re} \equiv \frac{n \cdot d_\mathrm{a}^2}{\nu} \tag{13}$$

where ν is the kinematic viscosity of the process fluid [29], [30]. The power characteristics $\mathrm{Ne} = f(\mathrm{Re})$ of each agitator setup were identified by simulation and are depicted in Fig. 15. In order to calculate the torque, for example, for a larger tank or for a fluid with higher viscosity, the torque can be scaled up for a similar geometry under the condition that Ne = idem and Re = idem [29], [30].

It arises that, at high Reynolds numbers $(\mathrm{Re} > 3 \cdot 10^5)$, the power number Ne can be considered as a constant. Thus, with (12), the necessary mixer torque can be stated as

$$T \propto n^2 \tag{14}$$

for a specific geometric mixer setup. In Fig. 16, the simulated load torque T caused by the process fluid is depicted in dependence on the rotational speed n at various mixer setups.

Another critical parameter is the fluid force F_z acting in the z-direction on the rotor because this DOF is only stabilized by reluctance forces (cf. Section II). If the force F_z exceeds a specific value (about 150 N), the rotor could be pulled off

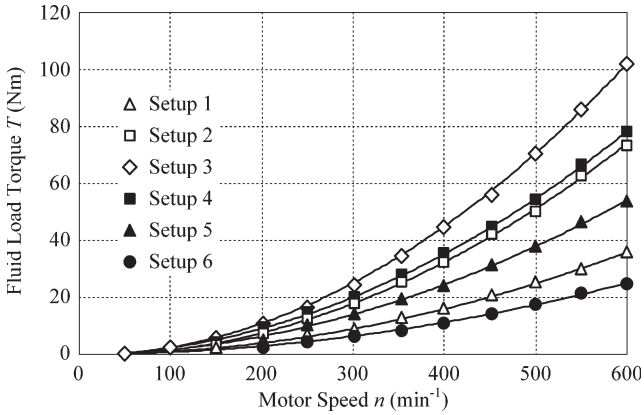

Fig. 16. Simulated load torque T in dependence on the agitator rotational speed n at various agitator setups (the parameters of the agitator setups are listed in Fig. 13).

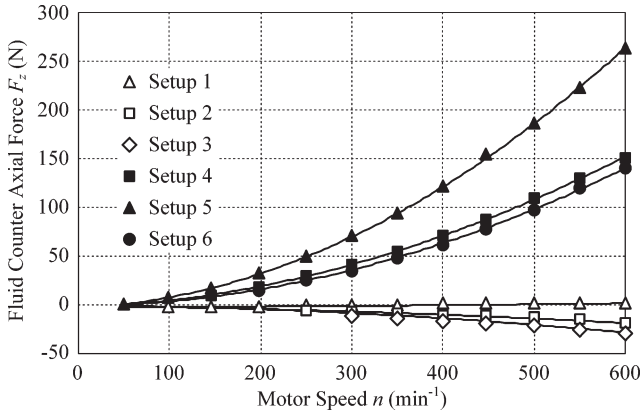

Fig. 17. Fluid counterforce acting on the agitator in z-direction (F_z) in dependence on the rotational speed n (the parameters of the agitator setups are listed in Fig. 13).

from the stator. Therefore, F_z was investigated during mixing operation. The results of this simulation are depicted in Fig. 17. As expected, the pitched-blade agitators, particularly the agitator with $\alpha_\mathrm{a} = 45°$, produce the highest axial force whereas F_z could be neglected when operating a flat-blade agitator.

Via this fluid simulation, it could be demonstrated that the introduced bearingless mixer motor provides sufficient torque to operate various agitators which comply to the design recommendations (10) and (11). Agitator setups 1, 2, 4, and 6 can be used without limitation up to the nominal speed of $n = 500\ \mathrm{min}^{-1}$. When operating with setups 3 and 5, the speed must be limited due to a too high value of T and F_z, respectively. For the forthcoming investigations, setup 2 was chosen because the fluid torque at $n = 500\ \mathrm{min}^{-1}$ is close to the maximal achievable mixer torque of $T = 54\ \mathrm{N \cdot m}$ and the occurring axial force F_z is quite low.

B. Verification

In order to verify the simulated data (torque T and axial force F_z), the prototype (cf. Fig. 18) was installed in a 300-L test vessel and was loaded with a four-wing flat-blade agitator according to setup 2 (cf. Fig. 13). The motor was operated in a speed range from 0 to 500 min^{-1}.

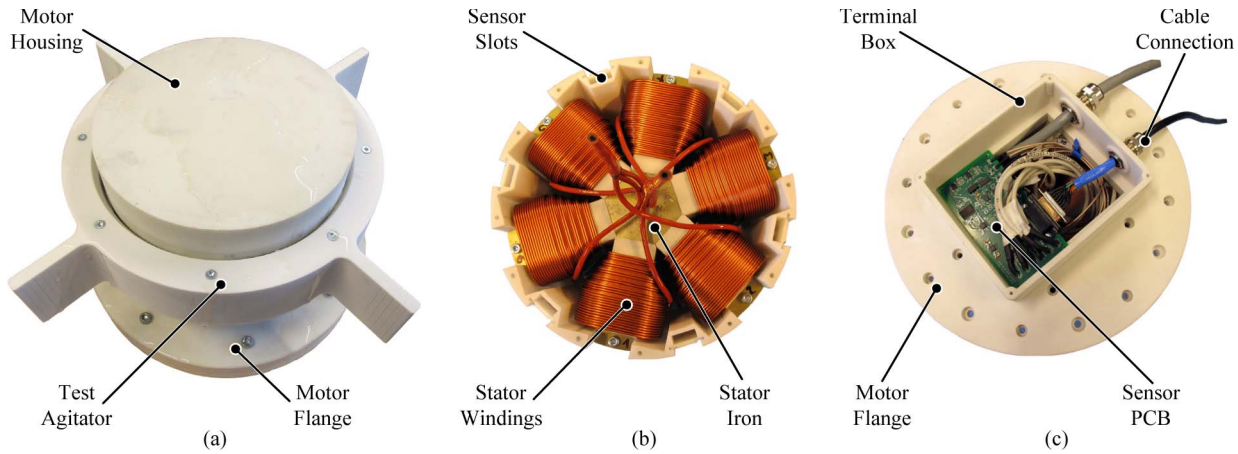

Fig. 18. Prototype setup. (a) Bearingless mixer motor with test agitator (cf. setup 2, Fig. 13). (b) Top view of semifinished motor showing stator windings and stator iron. (c) Bottom view of the prototype showing the sensor electronics.

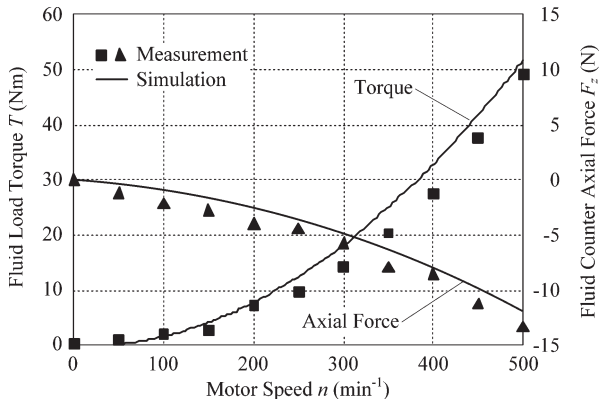

Fig. 19. Comparison of measured and simulated values of torque and axial force during mixing operation. The mixer was operated with a flat-blade agitator (cf. setup 2) in a 300-L test vessel.

Since, during mixing operation, T and F_z can be measured only with huge technical effort, the drive current I_{DRV} and the axial dislocation Δ_z of the rotor were recorded instead. The actual torque

$$T = 3 \cdot k_T \cdot N_{\mathrm{coil}} \cdot \hat{I}_{\mathrm{DRV}}$$

can be calculated according to (5), and the axial force

$$F_z = k_z \cdot \Delta_z \tag{15}$$

can be calculated with the axial stiffness k_z.

In Fig. 19, the simulated and the measured data are depicted. The experimental data show that the fluid simulation predicts the fluid forces quite well. At 500 min^{-1}, the measured load torque is about 50 N · m, and the rotor is dislocated less than $\Delta_z = 1$ mm in the z-direction.

VI. Thermal Simulation

Due to the exterior rotor design, the available construction volume for the stator and also for the stator windings is restricted. Therefore, the stator current density must be high to reach the targeted motor torque. To eliminate the danger of overheating during operation, a thermal simulation was implemented. Moreover, this simulation serves to examine if electronic components in the interior of the motor take damage during the SIP process at about 130 °C.

To set up a thermal simulation, all relevant heat sources in the motor must be investigated. The following three sources were identified: the iron losses in the laminated stator stack, the copper losses in the stator windings, and the eddy-current losses in the electrically conducting tank wall (placed between the rotor and the stator).

A. Iron Losses

The total iron losses P_{fe} in the laminated stator stack are composed of the eddy-current losses P_{ed} and the hysteresis losses P_{hy}. Since the flux density is not homogeneously distributed in the motor iron, the laminated stack is segmented into j parts so that, in each part i, the flux density $B_{\mathrm{fe},i}$ can be considered as constant [31]–[33] and the total iron losses can be stated as

$$P_{\mathrm{fe}} = \underbrace{c_{\mathrm{ed}} \cdot f_{\mathrm{el}}^2 \cdot \sum_{i=1}^{j} \hat{B}_{\mathrm{fe},i}(\Theta)^2 \cdot d_{\mathrm{fe}}^2 \cdot m_{\mathrm{fe},i}}_{P_{\mathrm{ed}}} + \underbrace{c_{\mathrm{hy}} \cdot f_{\mathrm{el}} \cdot \sum_{i=1}^{j} \hat{B}_{\mathrm{fe},i}(\Theta)^{\beta} \cdot m_{\mathrm{fe},i}}_{P_{\mathrm{hy}}}. \tag{16}$$

The flux density B_{fe} in the stator teeth is almost sinusoidal and alters with the electric frequency of the supply f_{el}. The coherence between the flux density magnitude $\hat{B}_{\mathrm{fe}}$ and the MMF Θ was determined by 3-D field simulation.

B. Winding Copper Losses

The second relevant loss source is the copper losses in the stator windings

$$P_{\mathrm{cu}} = 6 \cdot I_{\mathrm{DRV}}^2 \cdot R_{\mathrm{cu}}(\vartheta_{\mathrm{cu}}) \tag{17}$$

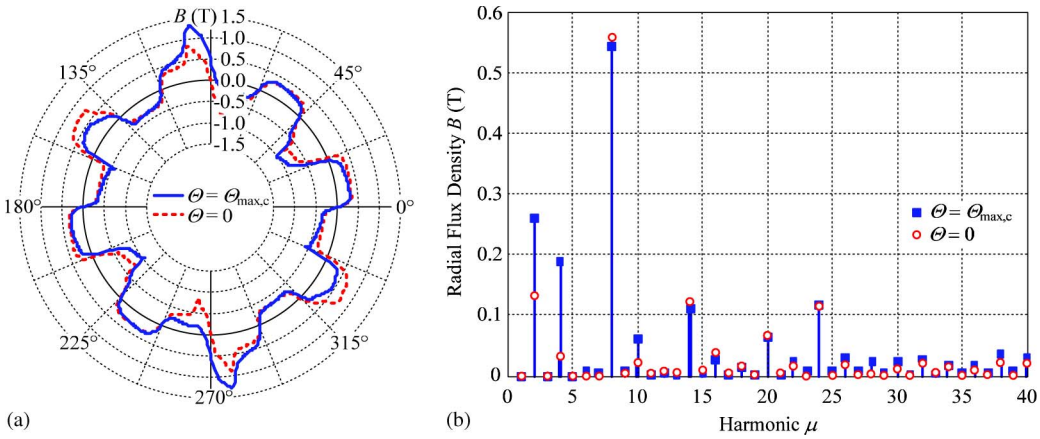

Fig. 20. (a) Simulated radial flux density B in the tank wall at no load ($\Theta = 0$) and at full load ($\Theta = \Theta_{\max,c}$), plotted in a stator fix reference frame at $z = h/2$ and $\alpha_{\mathrm{mech}} = 90°$. (b) Spectrum of the radial flux density B. The spectrum does not significantly vary with the rotational position α_{mech} of the rotor, and only the amplitudes of the second, the fourth, and the tenth harmonic significantly depend on the load.

where R_{cu} is the ohmic resistance of one of the six similar stator coils which are energized by the drive current I_{DRV}. Due to the significant increase of the winding temperature ϑ_{cu} during operation, the dependence of the resistance on the temperature is considered.

C. Tank Wall Losses

Since the tank wall is placed between the rotor and the stator of the mixer motor, the tank wall is locally penetrated by alternating magnetic fields. The tank wall is made of stainless steel which exhibits a significant electric conductivity. Hence, eddy currents are induced which cause ohmic losses in the wall.

In Fig. 20(a), the radial flux density at the location of the tank wall at $z = h/2$ is depicted. The flux density is not purely sinusoidal because of the presence of the six stator teeth. In Fig. 20(b), the spectrum of the radial flux density is depicted. Further simulations reveal that the coherence between the spectrum and the rotational position of the rotor α_{mech} is negligible and only the amplitudes of the second, the fourth, and the tenth harmonic significantly depend on the load.

With the knowledge of the flux density, the wall losses can be calculated. In [34] and [35], a mathematical model to estimate the wall losses in a screened motor is provided. This calculation is based on the assumption that the field penetrates the tank wall perpendicularly and the wall is thin enough to consider the field as constant throughout the radial dimension of the tank wall. In Fig. 21, the flow lines of the eddy currents caused by a sinusoidal harmonic of the radial flux density are depicted. Each harmonic μ of the radial flux density is defined by the amplitude $\hat{B}_\mu(\Theta)$, the electric angular velocity $\omega_{\mathrm{el},\mu}$, and the corresponding number of pole pairs p_μ. The according losses in the tank wall with the height $h_{\mathrm{wall}} = h \cdot (1 + \xi)$ (cf. Fig. 21) can be stated according to [34] as

$$P_{\mathrm{wall},\mu} = \frac{\sigma \cdot \delta_{\mathrm{wall}} \cdot D_{\mathrm{wall}}^3 \cdot h \cdot \pi \cdot \omega_{\mathrm{el},\mu}^2 \cdot \hat{B}_\mu^2(\Theta)}{8 \cdot p_\mu^2} \cdot K_\mu(\xi) \tag{18}$$

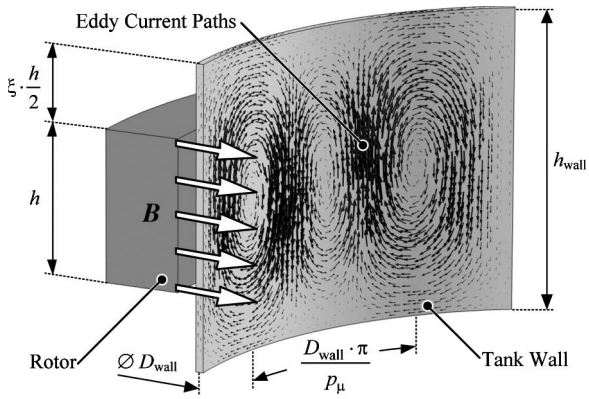

Fig. 21. Eddy-current pattern in the tank wall caused by sinusoidal radial flux density harmonic μ.

with the overhang correction factor

$$K_\mu(\xi) = 1 - \frac{\tanh\left(\frac{p_\mu \cdot h}{D_{\mathrm{wall}}}\right)}{\frac{p_\mu \cdot h}{D_{\mathrm{wall}}} \cdot \left(1 + \tanh\left(\frac{p_\mu \cdot h}{D_{\mathrm{wall}}}\right) \cdot \tanh\left(\xi \cdot \frac{p_\mu \cdot h}{D_{\mathrm{wall}}}\right)\right)}. \tag{19}$$

The dependence of the amplitude $\hat{B}_\mu(\Theta)$ on the MMF Θ was determined by a set of simulations.

To calculate the total eddy-current losses in the tank wall

$$P_{\mathrm{wall}} = \sum_\mu P_{\mathrm{wall},\mu} \tag{20}$$

all harmonic components of the flux density in the air gap must be considered [cf. Fig. 20(b)].

In Fig. 22, the wall losses in dependence on the overhang factor ξ are depicted. It arises that, at low overhangs ($\xi < 1$), the wall losses are increased by raising the overhang. For overhangs $\xi > 1$, the wall losses can be considered as constant. For forthcoming investigation, an overhang factor $\xi = 3$ was chosen since, in the real mixer setup, $h_{\mathrm{wall}} \gg h$ is true.

As mentioned earlier, the analytical calculation of the eddy currents in the tank wall was based on the assumption that the flux density, penetrating the tank wall, has only a radial

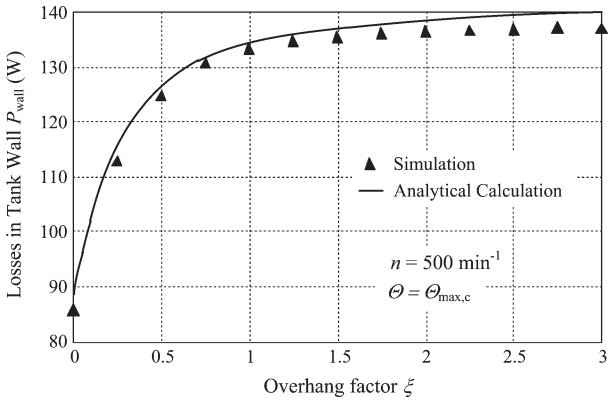

Fig. 22. Tank wall losses in dependence on the overhang. For overhang factors $\xi > 1$, the wall losses can be considered as constant. The calculation and simulation were done at $\Theta = \Theta_{\mathrm{max,c}}$ and $n = 500$ min^{-1}.

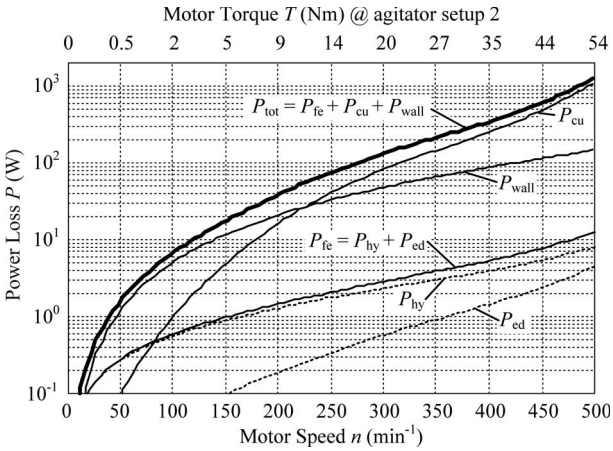

Fig. 23. Power losses in dependence on the motor speed. This evaluation is based on the agitator setup 2.

component [34], [35]. In order to verify this assumption for the case at hand, a 3-D FEM simulation was set up to compute the wall losses. In this simulation, also the tangential components of the flux density are considered. The results of the simulation are presented in Fig. 22. The simulated wall losses are close to the analytically calculated wall losses; thus, it could be proven that this assumption is justified.

D. Total Losses

In Fig. 23, the total losses

$$P_{\mathrm{tot}} = P_{\mathrm{fe}} + P_{\mathrm{cu}} + P_{\mathrm{wall}} \tag{21}$$

in dependence on the motor speed n are depicted. This evaluation is based on the load curve $T = T(n)$ from the agitator setup 2 (cf. Section V). Fig. 23 reveals that the stator iron losses are dominated by the hysteresis losses within the investigated speed range due to the low occurring frequencies. In comparison to the total motor losses, the stator iron losses are insignificant. The total motor losses are mainly composed of the wall losses and the winding copper losses, whereby the latter are dominating for speeds exceeding 250 min^{-1}. The iron losses of the rotor are not considered in this model because they

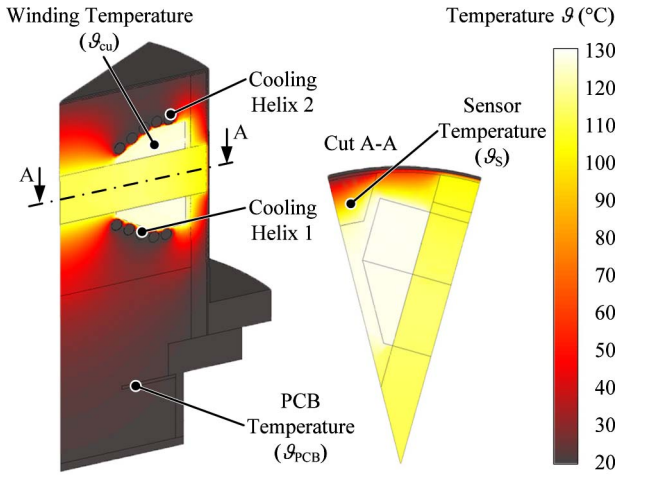

Fig. 24. Thermal FEM simulation of the mixer motor. Due to the axial symmetry of the mixer motor, only a 30° cutout is investigated. The picture shows the temperature distribution inside the motor. The motor is cooled by the surrounding process fluid and two cooling helixes placed directly above and below the winding.

TABLE I
SIMULATED TEMPERATURE AND MEASURED TEMPERATURE INSIDE THE MOTOR. MEASURED VALUES ARE GIVEN IN BRACKETS

Operating state	ϑ_{cu} (°C)	ϑ_S (°C)	ϑ_{PCB} (°C)	Status of water cooling
Permitted maximum temperature	130	125	85	
$T = 54$ Nm, $\Theta = \Theta_{max,c}$ $n = 500$ min^{-1}	123 (126)	72 (78)	27 (24)	helix 1 & 2 active
$T = 47$ Nm, $\Theta = \Theta_{max,sc}$ $n = 455$ min^{-1}	130 (133)	71 (78)	27 (25)	helix 1 active
$T = 32$ Nm, $\Theta = \Theta_{max,nc}$ $n = 410$ min^{-1}	130 (134)	75 (80)	38 (42)	no
SIP @ 130 °C	41	86	81	helix 1 & 2 active
SIP @ 130 °C	58	94	81	helix 1 active
SIP @ 130 °C	114	123	83	no

are very small and do not contribute to the temperature rise in the mixer due to the contactless suspension.

E. Thermal Simulation and Experimental Verification

In order to evaluate the temperatures during operation, a combined heat transfer–fluid simulation was set up (conjugated heat transfer [28]). The motor is cooled by the surrounding fluid and two additional water-cooling helixes. To realistically model the heat transfer into the tank fluid, the flow pattern presented in Section V was replicated. The simulated temperature distribution for a full load is depicted in Fig. 24. The most critical temperatures are the winding temperature ϑ_{cu}, the temperature of the position sensor ϑ_{S}, and the temperature of the PCB ϑ_{PCB}.

In Table I, the most important results are summarized. With both cooling helixes activated, the mixer motor can be operated up to the nominal motor speed of $n = 500$ min^{-1}. In this operation point, the torque is about $T = 54$ N · m (agitator setup 2), and the maximal MMF $\Theta = \Theta_{\mathrm{max,c}} = 5000$ At. is applied.

If only cooling helix 1 is activated, the maximal MMF must be reduced to $\Theta = \Theta_{\mathrm{max,sc}} = 0.7 \cdot \Theta_{\mathrm{max,c}}$, and if there is no

water cooling applied, the maximal allowable MMF is limited to $\Theta = \Theta_{\max,\mathrm{nc}} = 0.4 \cdot \Theta_{\max,\mathrm{c}}$ in order to keep the winding temperature below the maximal allowable value $\vartheta_{\mathrm{cu,max}} = 130\ ^\circ\mathrm{C}$.

Considering the agitator setup 2 (cf. Section V) with $\Theta = \Theta_{\max,\mathrm{sc}}$, the maximal possible motor speed is $n = 450\ \mathrm{min}^{-1}$, and a torque $T = 47\ \mathrm{N \cdot m}$ is achieved. With $\Theta = \Theta_{\max,\mathrm{nc}}$, the maximal possible speed is $n = 410\ \mathrm{min}^{-1}$ which results to a torque $T = 32\ \mathrm{N \cdot m}$ (cf. Table I). If the mixer should be operated at nominal speed without additional water cooling, an agitator design must be chosen which requires less torque (e.g., setup 5).

All components must be protected from overheating not only during operation but also during the sterilization process at 130 °C. In this operation state, the rotor is levitating, but no torque is requested. Therefore, the only significant heat source is the hot steam inside the tank. The simulation reveals (cf. Table I) that, during the sterilization of the tank, all temperatures are below the permitted maximum temperature, even if no additional water cooling is applied.

In order to verify the simulated temperatures, resistance temperature sensors (pt100 type) were placed in the motor before the assembly was potted. With these probes, the winding temperature, the position sensor temperature, and the PCB temperature were monitored during operation. The experimental results are also shown in Table I. Since the test tank was made of plastic, the experimental verification of the SIP process at 130 °C could not be executed so far.

With the fluid simulation presented in Section V and the thermal simulations presented in this section, it could be proven that the proposed bearingless motor produces sufficient torque to propel various agitators, and with water cooling, overheating during operation and sterilization is excluded.

VII. Conclusion

In this paper, a bearingless mixer motor with an exterior rotor ring has been presented. The motor is optimized for the usage in a 5000–10 000-L mixing facility. Based on fluid simulations and experiments, it could be proven that the motor with a nominal torque of $50\ \mathrm{N \cdot m}$ and a nominal speed of $500\ \mathrm{min}^{-1}$ is suitable for a wide range of agitator designs. Moreover, thermal simulations and measurements were conducted to verify that overheating of the motor is excluded during mixing operation and that the motor can withstand the high temperatures arising during the sterilization process. Finally, a prototype was set up and put into operation successfully.

References

[1] R. Schoeb and N. Barletta, "Principle and application of a bearingless slice motor," *JSME Int. J. Ser. C*, vol. 40, pp. 593–598, 1997.

[2] R. Schoeb, "Centrifugal pump without bearings and seals," *World Pumps*, vol. 2002, no. 430, pp. 34–37, Jul. 2002.

[3] S.-M. Yang and M.-S. Huang, "Design and implementation of a magnetically levitated single-axis controlled axial blood pump," *IEEE Trans. Ind. Electron.*, vol. 56, no. 6, pp. 2213–2219, Jun. 2009.

[4] T. Schneeberger, T. Nussbaumer, and J. W. Kolar, "Magnetically levitated homopolar hollow-shaft motor," *IEEE/ASME Trans. Mechatronics*, vol. 15, no. 1, pp. 97–107, Feb. 2010.

[5] J. A. Asenjo and J. C. Merchuk, *Bioreactor System Design*. New York: Marcel Dekker, 1995.

[6] Millipore, 2010, Dec. 9. [Online]. Available: http://www.millipore.com

[7] Y. Christi and M. Moo-Young, "Clean-in-place systems for industrial bioreactors: Design, validation and operation," *J. Ind. Microbiol. Biotechnol.*, vol. 13, no. 4, pp. 201–207, Jul. 1994.

[8] Y. Kai and F. Yaojing, "Design of novel spiral magnetic poles and axial-cooling structure of outer-rotor PM torque motor," *IEEE Trans. Appl. Supercond.*, vol. 20, no. 3, pp. 838–841, Jun. 2010.

[9] K. T. Chau, D. Zhang, J. Z. Jiang, C. Liu, and Y. Zhang, "Design of a magnetic-geared outer-rotor permanent-magnet brushless motor for electric vehicles," *IEEE Trans. Magn.*, vol. 43, no. 6, pp. 2504–2506, Jun. 2007.

[10] K. T. Chau, C. C. Chan, and C. Liu, "Overview of permanent-magnet brushless drives for electric and hybrid electric vehicles," *IEEE Trans. Ind. Electron.*, vol. 55, no. 6, pp. 2246–2257, Jun. 2008.

[11] M. Terashima, T. Ashikaga, T. Mizuno, K. Natori, N. Fujiwara, and M. Yada, "Novel motors and controllers for high-performance electric vehicle with four in-wheel motors," *IEEE Trans. Ind. Electron.*, vol. 44, no. 1, pp. 28–38, Feb. 1997.

[12] J. Chen, C. V. Nayar, and L. Xu, "Design and finite-element analysis of an outer-rotor permanent-magnet generator for directly coupled wind turbines," *IEEE Trans. Magn.*, vol. 36, no. 5, pp. 3802–3809, Sep. 2000.

[13] H. Lee, S. Chung, and S. Hwang, "Acoustic resonance of outer-rotor brushless dc motor for air-conditioner fan," *J. Appl. Phys.*, vol. 103, no. 7, pp. 07F116-1–07F116-3, Apr. 2008.

[14] K.-J. Han, H.-S. Cho, D.-H. Cho, and H.-K. Jung, "Optimal core shape design for cogging torque reduction of brushless dc motor using genetic algorithm," *IEEE Trans. Magn.*, vol. 36, no. 4, pp. 1927–1931, Jul. 2000.

[15] W. Amrhein, S. Silber, K. Nenninger, G. Trauner, M. Reisinger, and R. Schoeb, "Developments on bearingless drive technology," *JSME Int. J. Ser. C*, vol. 46, no. 2, pp. 343–348, Jun. 2003.

[16] S. Ye and K. T. Chau, "Chaoization of dc motors for industrial mixing," *IEEE Trans. Ind. Electron.*, vol. 54, no. 4, pp. 2024–2032, Aug. 2007.

[17] M. Ooshima, A. Chiba, T. Fukao, and M. A. Rahman, "Design and analysis of permanent magnet-type bearingless motors," *IEEE Trans. Ind. Electron.*, vol. 43, no. 2, pp. 292–299, Apr. 1996.

[18] T. Tera, Y. Yamauchi, A. Chiba, T. Fukao, and M. A. Rahman, "Performance of bearingless and sensorless induction motor drive based on mutual inductances and rotor displacements estimation," *IEEE Trans. Ind. Electron.*, vol. 53, no. 1, pp. 187–194, Feb. 2006.

[19] K. Raggl, B. Warberger, T. Nussbaumer, S. Burger, and J. W. Kolar, "Robust angle-sensorless control of a PMSM bearingless pump," *IEEE Trans. Ind. Electron.*, vol. 56, no. 6, pp. 2076–2085, Jun. 2009.

[20] T. Yamada, Y. Nakano, J. Asama, A. Chiba, T. Fukao, T. Hoshino, and A. Nakajima, "Outer rotor consequent-pole bearingless motor with improved start-up characteristics," *IEEE Trans. Magn.*, vol. 44, no. 11, pp. 4273–4276, Nov. 2008.

[21] T. Reichert, T. Nussbaumer, and J. W. Kolar, "Bearingless 300 W PMSM for bioreactor mixing," *IEEE Trans. Ind. Electron.*, to be published.

[22] T. Reichert, T. Nussbaumer, and J. W. Kolar, "Novel bearingless brushless motor in exterior rotor construction for stirred bioreactors," in *Proc. 5th IET Int. Conf. PEMD*, Apr. 2010, pp. 1–6.

[23] T. Reichert, T. Nussbaumer, W. Gruber, and J. W. Kolar, "Design of a novel bearingless permanent magnet motor for bioreactor applications," in *Proc. 35th Annu. Conf. IEEE IECON*, Nov. 2009, pp. 1086–1091.

[24] B. Warberger, T. Reichert, T. Nussbaumer, and J. W. Kolar, "Design considerations of a bearingless motor for high-purity mixing applications," in *Proc. SPEEDAM*, Pisa, Italy, Jun. 2010.

[25] K. Raggl, J. W. Kolar, and T. Nussbaumer, "Comparison of winding concepts for bearingless pumps," in *Proc. 7th ICPE*, Oct. 22–26, 2007, pp. 1013–1020.

[26] T. Reichert, T. Nussbaumer, and J. W. Kolar, "Torque scaling laws for interior and exterior rotor permanent magnet machines," in *Proc. Intermag*, Sacramento, CA, May 2009.

[27] Maxwell, *Electromagnetic Field Simulator*, Jan. 20, 2011. [Online]. Available: http://www.ansoft.com

[28] *Fluid Dynamics ANSYS CFX*, Jan 20, 2011. [Online]. Available: http://www.ansys.com

[29] M. Zlokarnik, *Rührtechnik Theorie und Praxis*. Berlin, Germany: Springer-Verlag, 1999.

[30] M. Zlokarnik, "Dimensional analyses and scale-up in theory and industrial application," *J. Liposome Res.*, vol. 11, no. 4, pp. 369–307, Dec. 2001.

[31] M. Bartholet, T. Nussbaumer, S. Silber, and J. W. Kolar, "Comparative evaluation of polyphase bearingless slice motors for fluid-handling applications," *IEEE Trans. Ind. Appl.*, vol. 45, no. 5, pp. 1821–1830, Sep./Oct. 2009.

[32] Z. Gmyrek, A. Boglietti, and A. Cavagnino, "Iron loss prediction with PWM supply using low- and high-frequency measurements: Analysis

and results comparison," *IEEE Trans. Ind. Electron.*, vol. 55, no. 4, pp. 1722–1728, Apr. 2008.
[33] Z. Gmyrek, A. Boglietti, and A. Cavagnino, "Estimation of iron losses in induction motors: Calculation method, results, and analysis," *IEEE Trans. Ind. Electron.*, vol. 57, no. 1, pp. 161–171, Jan. 2010.
[34] R. L. Russell and K. H. Norsworthy, "Eddy currents and wall losses in screened-rotor induction motors," *Proc. Inst. Elect. Eng.—A, Power Eng.*, vol. 105, no. 20, pp. 163–175, Apr. 1958.
[35] R. C. Robinson, I. Rowe, and L. E. Donelan, "The calculation of can losses in canned motors," *Power App. Syst. III, Trans. Amer. Inst. Elect. Eng.*, vol. 76, no. 3, pp. 312–315, Apr. 1957.

Bernhard Warberger received the M.Sc. degree in mechatronics from the Johannes Kepler University Linz, Linz, Austria, in 2008. He is currently working toward the Ph.D. degree in the Power Electronic Systems (PES) Laboratory, Swiss Federal Institute of Technology (ETH) Zurich, Zurich, Switzerland, working on high-torque bearingless motors for high-purity stirring applications.

From 2008 to 2009, he has been with Levitronix Gmbh, Zürich, developing power supplies for magnetically levitated pump systems.

Remo Kaelin was born in Zug, Switzerland, in 1984. He received the M.Sc. degree in electrical engineering and information technology from the Swiss Federal Institute of Technology (ETH) Zurich, Zurich, Switzerland, in 2011. During his studies, he has done research on high-speed electrical drive systems for medical and dental tools and on modular multilevel converters. For his master thesis, he focused on bearingless motors with exterior rotor design for high-purity mixing applications.

Since February 2011, he has been with BKW-FMB Energy AG, Bern, Switzerland, where he is currently working for the business unit of electrical power networks.

Thomas Nussbaumer (S'02–M'06) was born in Vienna, Austria, in 1975. He received the M.Sc. (with honors) degree in electrical engineering from the University of Technology Vienna, Vienna, in 2001, and the Ph.D. degree from the Power Electronic Systems (PES) Laboratory, Swiss Federal Institute of Technology (ETH) Zurich, Zurich, Switzerland, in 2004.

From 2001 to 2006, he has been with the PES, where he has done research on modeling, design, and control of three-phase rectifiers, power factor correction techniques, and electromagnetic compatibility. Since 2006, he has been with Levitronix GmbH, Zurich, where he is currently working on bearingless motors, magnetic levitation, and permanent-magnet motor drives for the semiconductor and biotechnology industry. His current research is focused on compact and high-performance mechatronic systems including novel power electronics topologies, control techniques, drive systems, sensor technologies, electromagnetic interference, and thermal aspects.

Johann W. Kolar (M'89–SM'04–F'10) received the Ph.D. (*summa cum laude*/promotio sub auspiciis praesidentis rei publicae) degree from the University of Technology Vienna, Vienna, Austria.

Since 1984, he has been working as an Independent International Consultant in close collaboration with the University of Technology Vienna in the fields of power electronics, industrial electronics, and high-performance drives. He has proposed numerous novel pulsewidth modulation converter topologies and modulation and control concepts, e.g., the VIENNA Rectifier and the three-phase ac–ac sparse matrix converter. He has published over 300 scientific papers in international journals and conference proceedings and has filed more than 75 patents. He was appointed Professor and Head of the Power Electronic Systems (PES) Laboratory, Swiss Federal Institute of Technology (ETH) Zurich, Zurich, Switzerland, on February 1, 2001. The focus of his current research is on ac–ac and ac–dc converter topologies with low effects on the mains, e.g., for power supply of telecommunication systems and More-Electric-Aircraft and distributed power systems in connection with fuel cells. Further main areas are the realization of ultracompact intelligent converter modules employing the latest power semiconductor technology (SiC), novel concepts for cooling and electromagnetic interference filtering, multidomain/multiscale modeling and simulation, pulsed power, bearingless motors, and power Micro Electro Mechanical Systems.

Dr. Kolar is a member of the Institute of Electrical Engineers of Japan and of the Technical Program Committees of numerous international conferences in the field (e.g., Director of the Power Quality Branch of the International Conference on Power Conversion and Intelligent Motion). From 1997 to 2000, he has been serving as an Associate Editor of the IEEE TRANSACTIONS ON INDUSTRIAL ELECTRONICS and, since 2001, as an Associate Editor of the IEEE TRANSACTIONS ON POWER ELECTRONICS. Since 2002, he has also been an Associate Editor of the Journal of Power Electronics of the Korean Institute of Power Electronics and a member of the Editorial Advisory Board of the IEEJ Transactions on Electrical and Electronic Engineering. He was the recipient of the Best Transactions Paper Award of the IEEE Industrial Electronics Society in 2005. He also received an Erskine Fellowship from the University of Canterbury, Canterbury, New Zealand, in 2003. In 2006, the European Power Supplies Manufacturers Association awarded the PES Laboratory of ETH Zurich as the leading academic research institution in Europe.